ACES Asian Chemical Editorial Society

doi.org/10.1002/cnma.202100201

CHEMNANOMAT
Full Paper

Special Collection

Active and Passive Motion in Complex pH-Fields

Nadir Möller,*[a] Sebastian Seiffert,[b] Thomas Palberg,[a] and Ran Niu[c]

Abstract: We create pH landscapes of increasing spatial complexity by placing ion exchange resin beads of different types and sizes in a closed cell featuring a negatively charged bottom substrate. We thus extend previous measurements in a chemically homogeneous background to investigations in chemically structured backgrounds, which evolve in time. We determine local pH gradients by photometry and study the resulting solvent flows along the substrate by tracking passive tracer particles. Analytical modelling of the dispersion of chemicals is possible for situations with dominantly diffusive transport. We then release phoretic swimmers in differently shaped pH fields and study their motion for selected examples. Catalytic Janus swimmers assembled in the wake of a mobile pH source form a modular swimmer showing a noise-dominated trajectory. For standard modular swimmers with passive cargo, we identify well-defined and reproducible swimming trajectory types at and around single pH sources. These include swimmer deflection and swing-by maneuvers, swimmer trapping and escape, as well as circular orbits. More complicated paths result from combining the pH fields of multiple pH sources. Finally, we address swimmer-swimmer interactions resulting from the superposition of their own pH fields. Our findings clearly demonstrate the high potential of chemically structured environments for swimmer steering. They can further be rationalized in a simple heuristic model considering the interplay of phoretic flows on different length and time scales and its influence on swimmer speed, orientation and emerging propulsion direction. In view of the vast range of possible combinations, our study has to remain preliminary. We anticipate, however, that it will aid the general understanding of transport experiments in pH-driven systems and other types of phoresis and thus also help design novel and useful strategies for directed transport on the micro-scale.

Introduction

Gradients of chemical potential along a solid surface in contact with a fluid induce a phoretic slip motion in or against gradient direction.[1,2] Prominent examples of phoretic effects include electro-phoresis related to electric potential gradients,[3,4] thermo-phoresis based on temperature gradients,[5–7] and diffusio-phoresis in concentration gradients.[2,8] In any case, the resulting slip velocity is proportional to the drop in chemical potential across the whole surface. Combination of phoretic surfaces with different extension (e.g. suspended mobile particles settled to a fixed substrate) introduces a fascinating wealth of possibilities of achieving fluid flow and particle transport. In particular, it facilitates phoretic swimming at the micro-scale without the use of moving parts. Autonomous micro-swimmers employ self-generated gradients of chemicals. The dispersion of chemicals from their source can be approximated as effectively diffusive at slow solvent flows, but advection is found to interfere at large solvent or swimmer velocities.[9] Most previous studies concentrated on single particle micro-swimmers like the famous catalytic rods or spherical Janus particles.[10–17] Here all relevant functionalities, like on-off switches, speed control, steering, etc., are integrated into a single unit. By contrast, modular micro-swimmers (as recently reviewed in)[18] are constructed by self-assembly of different components taking different functionalities. This offers the advantage that all functionalities can be optimized independently. pH driven variants of modular micro-swimmers have received attention as model systems, which readily yield to an *in situ* characterization of chemical conditions and solvent flows on all relevant length and time scales.[9,19] They minimally combine an ion exchange bead working as fuel source, and passive charged particles as cargo and propelling agent. In addition, the latter steer the swimmer by their arrangement.[20] Interestingly, swimmer assembly can be quantitatively understood in terms of effective pair potentials.[21] Moreover the involved phoretic propulsion mechanisms are well known and the resulting swimming motion can be described quantitatively by complementary theoretical approaches and corresponding simulations.[20,22–24]

Initially, investigations on diffusio-phoretic flows and motion concentrated on phoretic pumping and phoretic swimming in a stationary, chemically homogeneous background and centro-symmetric or rectified gradients. There, tracking of passive tracers yielded information on the phoretic solvent

[a] N. Möller, Prof. Dr. T. Palberg
Institute of Physics
Johannes Gutenberg Universität
Staudinger Weg 7, 55128 Mainz (Germany)
E-mail: namoelle@uni-mainz.de

[b] Prof. Dr. S. Seiffert
Department of Chemistry
Johannes Gutenberg Universität
Duesbergweg 10–14, 55128 Mainz (Germany)

[c] Prof. Dr. R. Niu
Huazhong University of Science and Technology
Luoyu Road 1037, Wuhan (P. R. China)

Supporting information for this article is available on the WWW under https://doi.org/10.1002/cnma.202100201

Special Collection *This manuscript is part of a special collection: "Beyond Active Colloids: From Functional Materials to Microscale Robotics".*

motion at the substrates[25] and aided full hydrodynamic modelling of the corresponding overall flow patterns.[26] Recently, however, attention turned to chemically structured and time dependent environments. These are typical in bio-systems and other systems with self-organized, spatially structured dynamics.[27–31] Chemically structured environments open an alternative route to internal steering of motion and transport as complementary to external guidance.[32–35] Understanding the chemotactic guidance of swimmers in such environments is a major challenge.[36] However, in the long run, it appears to be a necessary requisite to overcome the limited access of external steering to the inside of living systems. Recent theoretical investigation explored the chemotactic response of individual passive and active colloids to complex chemical gradients.[34,37–41] Reports on corresponding experimental work are, however sparse.[42,43]

We here present a first systematic overview on *modular* micro-swimmers in complex pH-landscapes of prescribed structure. First, we construct and quantify spatio-temporal pH landscapes of increasing complexity. We combine fixed and mobile, single and multiple pH gradient sources. We further combine anion exchange with cation exchange, both coupling to the solubility and dissociation equilibria of CO_2. For characterization, we connect height averaged local pH gradients from photometry[9] to the resulting local solvent flows obtained from observing passive tracers.[26] In the second part of the paper, we then present a collection of representative examples for phoretic swimming in such pH fields. Here, we study active Janus swimmers in the flow field created by mobile pH sources. Together, these form a modular swimmer showing noisy trajectories. We then release standard modular micro-swimmers (formed from mobile pH sources and passive particles) into different prescribed environments and study their trajectories. We demonstrate the influence of deliberately distributed pH sources on the swimmer motions. We realize trajectories showing deflection from pH sources generating an outward solvent flow along the substrate. At pH sources generating an inward solvent flow along the substrate, we observe swing-by maneuvers, swimmer trapping and escape as well as self-organized stable circle swimming. We also exploit the fact that our modular swimmers comprise a cationic ion exchange resin bead. They are thus themselves mobile pH sources generating an inward solvent flow. For the first time, we give examples of the mutual interaction between modular swimmers with standard passive cargo.[23] Finally, a consistent qualitative understanding of the observations on paths is obtained. To that end, we employ a heuristic extension of the established mechanisms of modular micro-swimming to chemically inhomogeneous environments. This extension takes into account the subtle interplay of hydrodynamic flows on different length scales and from different pH gradient sources. To be specific, we discriminate i) the flows generated locally at the modular swimmers and ii) the superposed solvent drift generated by the long-range pH gradients resulting from deliberately placed pH sources or from other swimmers. By modifying the geometry (i.e. the cargo arrangement) of the modular swimmer, the latter also change the orientation of the phoretic slip driving the swimmer. They thus govern the resulting trajectory, leading to an effective attraction or repulsion to or from large scale gradient sources.

In what follows, we first introduce the system chemistry, then present our samples, their conditioning and outline the employed experimental techniques. We then present the results of experiments on pH landscape design and swimmer motion within these. In the discussion section, we rationalize our findings in terms of our heuristic model and consider possible future extensions and applications. We close with some short conclusions.

Concepts, Methods and Materials

Ion exchange

Ion exchange (IEX) generates the gradients for phoretic pumping and propulsion. This works well, even in nominally salt free water due to presence of dissolved carbon dioxide. We explicitly note that the here established so-called realistic salt free conditions do not imply the absence of any ions. Rather, there still are the counter-ions of any added particle or surface (here assumed to be H^+) and further ions from different sources. These include residual stray ions (e.g. Na^+ or K^+), H^+ and OH^- (from water hydrolysis), as well as H^+, bicarbonate anions HCO_3^-, and neutral carbonic acid molecules H_2CO_3, from the atmospheric CO_2 contamination.

Exchangeable cations (Na^+ and K^+) either stem from the glass substrate or are left over from the washing procedures. These dissolve under reaction with CO_2 to form alkali carbonates. For cleaning protocols and boundary conditions close to the ones employed here, Niu et al. had estimated their concentration to be 10^{-8} to 10^{-7} mol L^{-1}.[19] This is low enough to exclude any influence on the carbonate dissociation equilibrium.[44,45] At cationic-IEX (CIEX) resin beads, salt cations, B^+, are exchanged for protons forming an acid with the residual anion, A^-:

$$R-H+A^-B^+ \Rightarrow R-B+A^-H^+ \tag{1}$$

where R denotes the polymeric resin backbone. It results in a surplus of acid close to the IEX, dispersing *via* diffusion. For sodium-bicarbonate:

$$R-H \;+\; Na^+ + HCO_3^- \Rightarrow R-Na \;+\; H^+ + HCO_3^- \tag{2}$$

we obtain a surplus of carbonic acid close to the resin, which is part of the dissociation scheme of CO_2. The carbonate related chemical reactions in the realistic salt-free aqueous solution are:

$$\begin{aligned} H_2O &\underset{K_{-1}}{\overset{K_1}{\rightleftharpoons}} H^+ + OH^- \\ H_2CO_3 &\underset{K_{-2}}{\overset{K_2}{\rightleftharpoons}} H^+ + HCO_3^- \\ H_2CO_3 &\underset{K_{-3}}{\overset{K_3}{\rightleftharpoons}} CO_2 + H_2O \end{aligned} \tag{3}$$

K_i and K_{-i} ($i=1, 2, 3$) are the corresponding forward (s^{-1}) and backward (s^{-1}) kinetic constants. According to the solubility and partial pressure of CO_2 in standard air at 25 °C, the concentration of CO_2 in realistic salt free water is 1.18×10^{-5} mol L^{-1}, which amounts to pH ≈ 5.5. Note, however, that this equilibrium may shift depending on the temperature and pressure of the system. Also the presence of salts or acids influence the equilibrium.[42,43] The surplus of carbonic acid locally leads to a pH below 5.5. It can distribute diffusively and can decay through successive reaction. We therefore expect an increase of pH with increasing distance from the CIEX center.

At the anionic IEX (AIEX) resin beads, anions are exchanged for OH^-. Anions are e.g. supplied by carbonic acid, in which case OH^- recombines with H^+, while the carbonic acid is supplemented from the store of neutral CO_2 through the reactions described in Eqn (3). Alternatively, carbonate can be supplied by inward diffusion of metal carbonates. The resulting metal hydroxide then reacts with carbonic acid.

$$\begin{aligned}
&R-OH+H^+HCO_3^- \underset{K_{-4}}{\overset{K_4}{\rightleftharpoons}} R-HCO_3+H_2O\\
&R-OH+Na^+HCO_3^- \underset{K_{-5}}{\overset{K_5}{\rightleftharpoons}} R-HCO_3+Na^+OH^-\\
&R-OH+Na^+Cl^- \underset{K_{-6}}{\overset{K6}{\rightleftharpoons}} R-Cl+Na^+OH^-\\
&Na^+OH^-+HCO_3^-H^+ \underset{K_{-7}}{\overset{K_7}{\rightleftharpoons}} H_2O+Na^+HCO_3^-
\end{aligned} \quad (4)$$

Where the K_i and K_{-i} ($i=1, 2, 3$) are again the corresponding kinetic constants. With ion exchange, the pH of a realistic salt free suspension will increase from an initial pH of 5.5 to 7 in the vicinity of the AIEX. In the case of added salt, (e.g. *NaCl*) a surplus of *NaOH* is formed and we expect an increase of pH to values pH > 7. Again, the surplus can distribute diffusively and can decay through successive reaction. We therefore expect a decrease of pH with increasing distance from the AIEX center.

In the present study, we will subject negatively charged surfaces in contact with aqueous electrolyte to a gradient in pH generated through the above mentioned reactions. This induces phoretic slip motion along the respective surfaces. If the surface is kept stationary, we obtain a phoretic or electro-osmotic pump (eo-pump). If the surface is mobile with respect to the stationary solvent, we obtain electro-phoretic motion of the particle. If, in addition, the particle itself generates the gradient, we have a phoretic swimmer. In both cases, mainly the gradient strength and direction, as well as surface zeta potential determine the resulting slip direction and velocity.

Gradients are formed mainly by diffusive dispersion of produced or exchanged chemicals (e.g. carbonic acid for CIEX). The resulting height averaged pH gradients are well described by a simple diffusion-advection model (see supplementary electronic materials) as long as an advective contribution to the transport of chemicals is small as compared to the diffusive contribution. In fact, our simple model[9] accounts for the flows *via* an enhanced diffusivity. In general, advection is introduced by the phoretic solvent flows along the substrate (convergent for CIEX and divergent for AIEX) and the corresponding counter-flows at approximately mid cell height. For the case of pumps made from small CIEX beads (e.g. CIEX45, see next section), these were previously determined in simulations.[26] Modelling of the dispersion of chemicals has further been adapted to swimmers propelling at constant speed and pumps in a stationary homogeneous solvent flow. Using the extended model we successfully described the pH gradient evolution around small IEX beads both in pumps and in swimmers.[9] As we will show in the results section of the present paper, the model also works well for large advective components, given the flow field is homogeneous. It fails for large IEX, where chemicals are dominantly provided by solvent advection and the production rate rises above its diffusion controlled value.

Materials

Table 1 gives an overview of all system components used and combined in this study on pH gradient driven phoretic motion for different tasks. We give both the batch codes of the manufacturers and the Lab codes encoding particle type and size used throughout this paper. Diameters were determined from optical microscopy.

We combine these components in experiments of increasing complexity. These comprise: i) Simple low and high throughput electro-osmotic (eo) pumps (CIEX45, CIEX-L, AIEX-L). ii) Combinations of like and unlike eo-pumps (CIEX-L, AIEX-L). iii) Freely propelling simple modular swimmers made from a single

Table 1. System components used and combined in this study on pH gradient driven phoretic motion for different tasks.

Type of component	Task	Batch number	Labcode	Diameter/μm	References
charged Polystyrene sphere	tracer	PS/Q-F-L1214	PS9	9,3	[23]
charged Polystyrene sphere	tracer, cargo	PS/Q-F-KM191	PS14	14,4	[23]
charged Polystyrene sphere	tracer, cargo	PS/Q-F-L1488	PS15	15,2	[23]
charged Polystyrene sphere	tracer, cargo	PS/Q-F-L2619	PS20	20,1	[23]
Pt@PS Janus sphere	swimmer, cargo	–	J3, J5	3 5	[38]
Resin based cation exchanging sphere	modular swimmer	CK10S	CIEX15	15,3	[23]
Micro-gel based anion exchanging sphere	modular swimmer, eo pump	CGC50×8	CIEX45	45	[23]
Resin based cation exchange sphere	eo-pump	Amberlite K306	CIEX-L	467–507	[46]
Resin based cation exchange splinters	modular swimmer	Amberlite K306	CIEX-Splinter	< 300 μm	[22]
Resin based anion exchange sphere	eo-pump	Amberlite K306	AIEX-L	480–533	[46]
HC III soda lime glass	substrate				[45]

CIEX and PS cargo (PS@CIEX45; PS@CIEX-Splinter). iv) Simple swimmers in a flow field. v) Simple modular swimmers in the vicinity of high throughput eo-pumps (PS@CIEX45, CIEX-L AIEX-L). vi) Two interacting simple swimmers (PS@CIEX45; PS@CIEX-Splinter). vii) Simple swimmers made of CIEX45 and active J3 cargo. In all cases the basic mechanisms, driving pumping and propulsion of the modular swimmers, are based on ion exchange.

Sample preparation

All experiments are performed in custom-built observation cells, constructed from circular Poly-Methyl-Methacrylate (PMMA; Perspex®) rings with inner radius of $R = 12.5$ mm attached to a microscopy slide by hydrolytically inert epoxy glue (UHU plus sofortfest, UHU GmbH, Germany) and dried for 24 h before use. Standard ring height was $H \approx 0.5$ mm, slightly varying with glue layer thickness. Commercial soda lime glass slides of hydrolytic class 3 (VWR International, Germany) served as substrates. These were washed with 1% alkaline solution (Hellmanex®III, Hellma Analytics) under sonication for 30 min, then rinsed with tap water and subsequently washed with doubly distilled water for several times. Substrate surface potentials were determined using Doppler velocimetry under realistic salt free conditions.[23] Their zeta potential was $\zeta = -138.2 \pm 8.0$ mV, corresponding to an electro-osmotic mobility of $\mu_{eo} = 11.0 \pm 0.7$ μm/s/V/cm. In addition, cells built using Perspex® slides ($\zeta = -58.7 \pm 4.4$ mV, $\mu_{eo} = 4.8 \pm 0.4$ μm/s/V/cm) were used.

Different types of ion exchange resin are used. To assemble modular swimmers, we employed micro-gel based cationic ion-exchange resin spheres of diameters $2a = 45 \pm 1$ μm obtained by image analysis (CIEX45; CGC50×8, Purolite Ltd, UK). These were soaked in 1.2 mol/L HCl for a few hours. After acid regeneration, the beads were thoroughly washed with milli-Q water. For swimmers with Janus cargo, we employed smaller resin based, pre-conditioned CIEX (CIEX15; CK10S, Mitsubishi Chemical Corporation, Japan) with diameters of (15.3 ± 3.0)μm, which were used as provided. To generate large scale pH and flow fields, we employed the beads of commercial nano-porous resin based mix-bed ion exchanger (CIEX-L and AIEX-L; Amberlite *K306*, Roth GmbH, Germany). Cation- and anion exchange beads were separated and each batch rinsed with milli-Q water. Sizes determined by microscopy ranged from 467 μm to 507 μm for CIEX-L and 480 μm to 533 μm for the AIEX-L. IEX beads were glued to the substrate at chosen locations. The cell was then covered by a second microscopy side (either glass or Perspex®) bearing two small holes, to avoid contamination by dust and simultaneously allow maintaining equilibration with ambient CO_2. Through these, we subsequently fill the cell with colloidal particle suspension without remaining bubbles.

Suspensions were prepared from distilled water, colloidal particles and, if desired, small IEX and/or appropriate amounts of analytical grade *NaCl* (Art. 9265.1, Roth GmbH, Germany). Particles and resins quickly sediment to the cell bottom after filling. The suspensions also contained a small amount of a diluted mixture of two standard pH-indicator fluids (pH 4.0–10.0 Universal Indicator, MERCK; pH 0–5.0 pH-indicator solution, Sigma Aldrich). This yields an indicator concentration of 200–500 μmol L^{-1}, which provides good color contrast over a large pH range but is low enough to avoid interference with swimming performance. Passive colloid particles are used either as cargo for modular swimmers (in the presence of small CIEX) or as tracers. Here we relied on sulphate stabilized polysterene microspheres with diameters 9.3 μm, 14.4 μm, 15.2 μm or 20.1 μm as determined from TEM measurements (PS/Q-F-L1214, PS/Q-F-KM191, PS/Q-F-L1488 or PS/Q-F-L2619, Microparticles GmbH, Germany). These show an electro-phoretic mobility of $\mu_{ep} = (-2.1 \pm 2)$ μm/s/V/cm independent of sphere size. To assemble "tumbling" modular swimmers, we used Pt coated silica spheres (J3 and J5). These were kindly provided by Larysa Baraban, and their preparation and conditioning has been described elsewhere.[46] Without added H_2O_2 they perform like passive cargo. With added H_2O_2, they perform as active cargo and significantly alter the swimmer performance. To characterize their activity, we studied their free motion with and without added H_2O_2. This is shown in Figure 1a and b, where we display two selected trajectories recorded over 60s and the mean squared displacement calculated thereof for three different

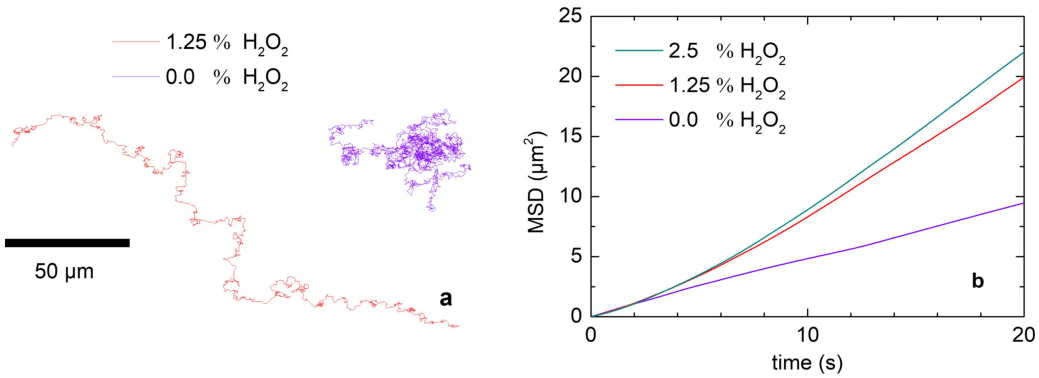

Figure 1. Characterization of Janus particles. a) Trajectories of freely suspended J3 on a glass substrate at H_2O_2 concentrations of 0 and 1.25%, respectively. Trajectories were recorded using particle tracking over 60s b) Mean squared displacement (MSD) as derived from tracking measurements at different H_2O_2 concentrations as indicated in the key. With added H_2O_2 the MSD increases quadratically with time.

H_2O_2 concentrations. (An additional trajectory recorded at $c_{H2O2} = 2.5\%$ is shown in Figure S6a of the supplement.) At realistically salt free conditions, a concentration of $c_{H2O2} = 1.25\%$ suffices to introduce directed propulsion with an average velocity of $v \approx 4$ μm/s in a reproducible way.

Particle tracking and pH mapping

After filling the cell with IEX beads and cargo particle suspension, the modular swimmers self assemble, start propelling, pick up cargo one by one and further accelerate.[23] We monitor motion of active and passive particles by video tracking and the concentration of carbonic acid *via* high-resolution pH mapping. We mount the cell to the x-y-stage of an inverted microscope (DMIRBE, Leica, Germany) allowing for uniform Köhler illumination ($\Delta I(x,y)/<I> \leq 0.015$) and observation in transmission with two cameras simultaneously. A standard video camera at 60fps records tracking videos at 5× or 10× magnifications. Videos are analyzed using custom written tracking algorithms.[23] An example is shown in Figure 1a.

For pH determination, we observed the sample with a consumer DSLR (D700. Nikon, Japan) using a 0.63× mounting tube. The camera features a FX-format CMOS sensor (36.0× 23.9 mm^2) with 4.256×2.832 = 12.87 Mpix on the sensor, arranged in a Bayer pattern for the three channels resulting in four pixel dots, defining the maximum spatial resolution. We convert the initially captured 14-bit RAW format to TIFF for further processing. A custom written python script achieves pixel-wise splitting of the intensity readings of each colour channel (RGB).[47] For each channel, we bin the data in blocks containing 6×6 pixels of the same channel. We then calculate the block mean absorbance, *A*, in each channel, using Beer-Lambert's law. For each two channels, the two channel absorbance ratio is proportional to the local pH. Calibration of absorbance ratios by indicator mixture in buffer solutions yielded an uncertainty in pH determination of ~0.02 pH units for pH values between 1.9 and 8.9. The quantitative evaluation of profiles and slopes is performed in custom written python scripts and fit routines. Here, the pH resolution combines with the spatial resolution from block-wise binning to result in a gradient resolution of ~0.02 pH units/6 μm.

For pH map design, a color rendering developed in OriginLab 9.0® was employed. For reasons of clarity, we here reduced the pH resolution of the color-coding to intervals of 0.2 pH units. Note that the coding corresponds to the absorption ratio, i.e. regions of low pH have a strong blue absorption are rendered blue, while the corresponding transmission image appears yellowish. Further, the displayed pH maps are spatially resolved into 357×237 blocks. At 10× (5×) magnification, each block covers an area of 5.8×5.8 μm^2 (11.6×11.6 μm^2) and the image size is 2072×1375 μm^2 (4144×2750 μm^2). Examples of pH maps and distance dependent velocities around low throughput eo-pumps have been already shown in previous work as well as their theoretical analysis. To illustrate the pH-determination method we here repeated previous experiments[9] using a simple PS15@IEX45 swimmer during successive cargo pick-up and acceleration in Figure 2. Note the excellent resolution obtained in terms of both position and pH (see also Videos 1 and 2 in the electronic supplementary material).

Results

Single eo-pumps

We will start with the characterization of height-averaged pH fields and the flow fields around single, stationary ion exchange beads (eo-pumps) of different sizes (CIEX45 and IEX-L). However, it appears instructive to shortly recall our previous findings and data treatment for low-throughput pumps,[9] before showing the results of the present experiments. Around single pumps, the emerging pH-field is concentric about the IEX beads, and due to the closed cell geometry, it evolves with time. The dominating chemical species is carbonic acid. At any time, *t*, the measured height averaged radial pH profile were excellently described using the solution of the advection-diffusion equation for a stationary source. Fits of this model then returned a constant production rate, μ^+, a decay rate, μ^-, depending linearly on concentration and an effective diffusion coefficient, D_{eff} for carbonic acid. The latter accounts for advection effects in an effective way. It typically was found to be somewhat smaller than the free (Nernstian) diffusion coefficient ($D_{Nernst} = 2096\ \mu m^2 s^{-1}$) and decreases with increasing substrate charge, i.e. with increasing phoretic pump flow. The decrease thus was attributed to a small advective contribution to the dispersion of chemicals. Importantly, the height-averaged pH is not identical to the pH at typical tracer/swimmer level. In fact, the derived height averaged gradients are much weaker than at the tracer/swimmer level. For low throughput pumps, the latter could be calculated analytically using the parameters describing the height averaged pH as input.[9] For further details of the theoretical treatment and data analysis, we refer the interested reader to the short summary given in the electronic supplementary materials and the extended descriptions in [20] and [9].

Earlier work on high-throughput IEX did not include any pH measurements. To facilitate a comparison between low- and high-throughput pumps we first repeated the experiment on CIEX45 of our previous study,[9] then investigated the pH fields around high-throughput CIEX-L and AIEX-L.

For the pH field of the CIEX45, the present experiments reproduce the behavior seen in previous studies.[9,19] In Figure 3a, we show a typical profile for a CIEX45 pump on glass as recorded at $t = 200$s (blue diamonds). Note the excellent data quality due to radial averaging and the near perfect description of the profile by a two parameter fit yielding a production rate of $\mu^+ = (127 \pm 10)\ mol\,L^{-1}\,s^{-1}$ and a maximum inward solvent velocity $v_{eff} = 4.1\ \mu m\,s^{-1}$. (Here, all other parameters were fixed to values determined in independent experiments on PS20@CIEX45: $D_{eff} = 1585\ \mu m^2 s^{-1}$, $\mu^- = 1.2 \times 10^{-3}\ s^{-1}$, and $c_\infty = 3.1\ mol\,L^{-1}$). For small AIEX working under realistic salt free conditions, the pH close to the AIEX surface takes values of

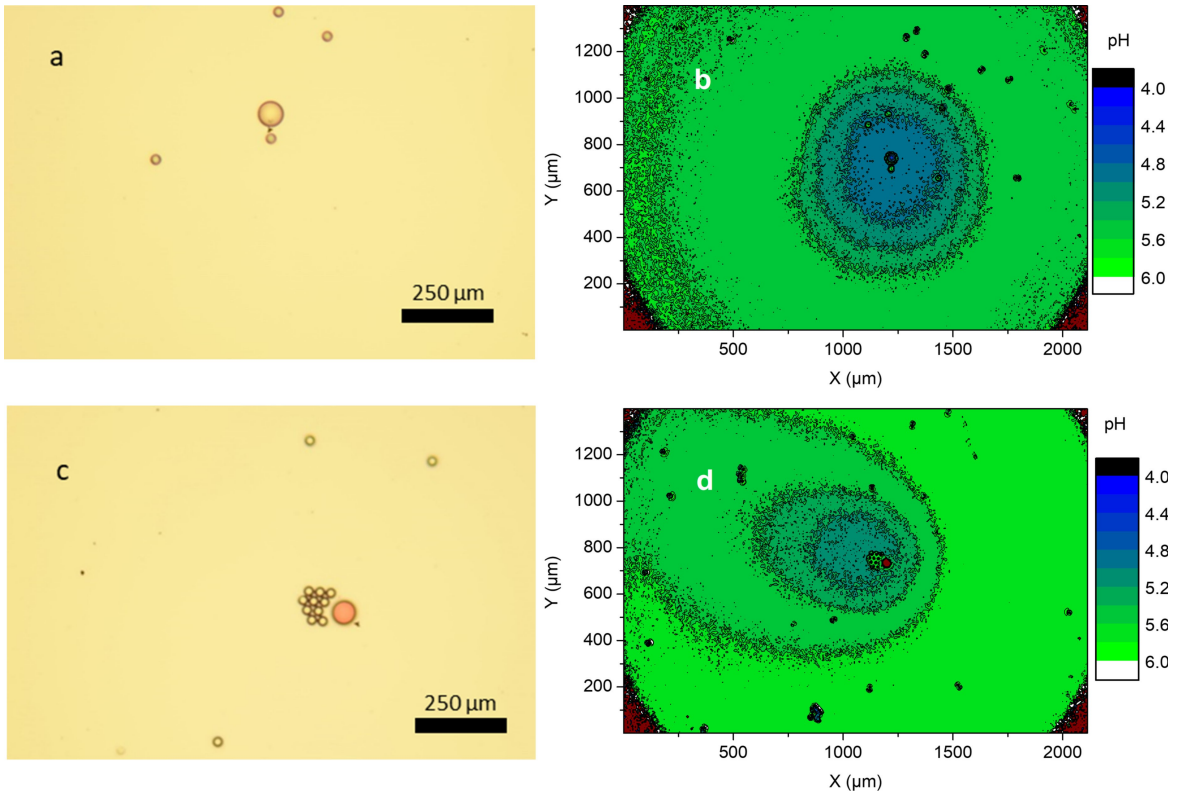

Figure 2. Modular swimmer (PS15@IEX45) at two different times after formation. Top row: $t = 60$s, one cargo, speed v = 1.8 µm/s. Bottom row: the same swimmer after several cargo pick-ups. $t = 410$s, 10 cargo, speed v = 5.2 µm/s. Left side (a and c) shows the microscopic images with scale bar 250 µm. Right side (b and d) shows the corresponding pH-maps with color coding as indicated in the key. Note the elongated shape of the ellipsoidal pH trail.

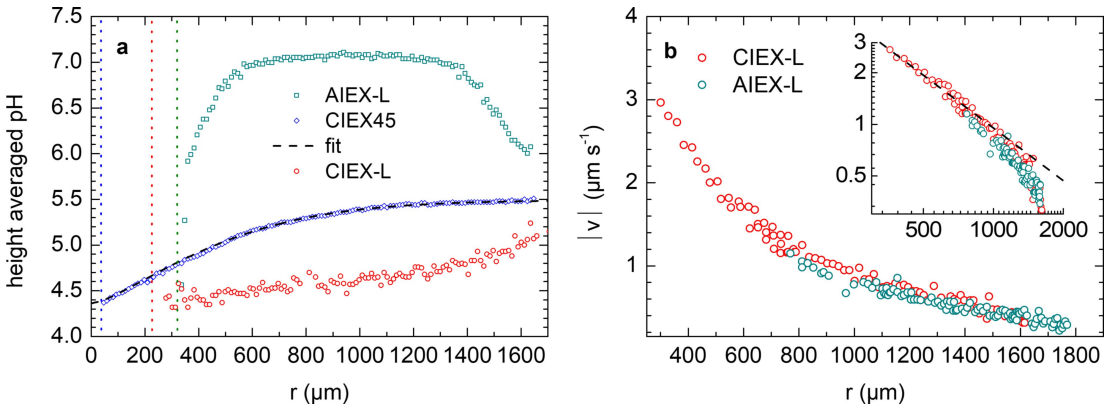

Figure 3. Selected radial pH-profiles for differently sized eo-pumps working in realistically salt free conditions on a glass substrate. a) Comparison of pH-profiles obtained at stationary beads of CIEX45 (low throughput, blue diamonds), CIEX-L (high throughput, red circles), and AIEX-L (high throughput, olive circles) for $t = 200$s. Note the qualitatively different shapes. Only the profile of CIEX45 can be theoretically described. From the fit we obtain a production rate of $\mu^+ = (127 \pm 10)\ \mathrm{mol\,L^{-1}\,s^{-1}}$ and a maximum inward solvent velocity $v_{\mathrm{eff}} = 4.1\ \mu\mathrm{m\,s^{-1}}$, with all other parameters known from independent experiments. b) Moduli of tracer velocities as measured for CIEX-L (red) and AIEX-L in the region of the outer pH-profile slope (cyan). Both measurements were performed after attainment of stationary pH-profiles (30 min). Inset: double-logarithmic plot of the data.

pH = 6–7 (not shown). Surface values above 7 are obtained in the presence of neutral salt, from which accumulating alkali hydroxide B^+OH^- is formed upon anion exchange. Irrespective of salt concentration, the pH values drop towards the far field pH. Correspondingly, the tracer velocity is outward, demonstrating the divergent solvent motion along the substrate.

The situation is markedly different for high-throughput pumps of both types. Figure 3a, also displays typical data recorded at $t = 200$s for CIEX-L (red) and AIEX-L (cyan). Data are restricted to r-values larger than the IEX radii. (The region covered by the IEXs also shows interesting color changes, but cannot be securely evaluated in terms of an average pH due to

the optical absorption of the IEX material itself (c.f. Figure S3 in the electronic supplement). The three curves differ qualitatively.

For CIEX-L, the initial pH increase with subsequent saturation at the far field value has shifted outward. The inner profile is now characterized by weak, near linear pH increase of constant slope. According to our reaction scheme, this corresponds to the accumulation of carbonic acid next to the CIEX and a slow conversion to CO_2. At the CIEX surface values of pH $\approx$4.2–4.5 are observed. Only at large distances, the pH increases dominantly due to diffusive dispersion of carbonic acid. The enhanced production rate of carbonic acid is attributed to the inflow of fresh alkali carbonates along the top substrate.

Also for AIEX-L, the typical pH-decay has shifted considerably outward. In the intermediate region, we observe an extended plateau at pH$\approx$7, indicating a zone, nearly free of carbonic acid. Again, this is attributed to the advective inward transport of exchangeable chemicals. In the center atop the IEX, the flow bends downward due to solvent incompressibility. Both fresh carbonic acid and alkali carbonates are accumulated. The pH drops towards the far field value pH = 5.5. In outward direction, we therefore observe a narrow transition towards pH $\approx$7 in the plateau region. The inner positive gradient is linear and very steep. This is attributed to the rapid decay of carbonic acid by both direct conversion to CO_2 and its neutralization by reaction with alkali hydroxide resulting from the ion exchange of alkali carbonates (c.f. Eq. 4). Hence, AIEX surroundings beyond $r\approx$500 μm are left pH neutral. A depletion zone is formed. Only at large distances, the pH drops again due to diffusive supplement of carbonic acid.

Moreover, both pH-profiles display a marked initial evolution. For CIEX-L the region of linear increase shifts towards the outer cell boundary. The same occurs for AIEX-L with the outer boundary of the plateau region. Both evolution and long-term fate additionally depend on the initial salt concentration. For more details on these points, the interested reader is referred to the supplementary material. In the present context, however, it may suffice to note that after about half an hour a region of radius r$\approx$2 mm has acquired a stationary pH profile. Stationary or still evolving, none of the IEX-L pH-profiles can be described by our analytical model.[9] This is due to a mismatch of the boundary conditions of the experiment and those assumed in the model. Height averaged pH gradients can only be described only as long as the advective contribution to the supply of exchangeable chemicals is small as compared to the diffusive dispersion of the products.

We next turn to the corresponding solvent flow fields along the bottom substrate as determined from the tracer experiments. Figure 3b compares the distance dependent moduli of tracer velocities as measured in the stationary state for CIEX-L (tracers moving inward) in the region of linear pH increase and for AIEX-L in the plateau region from r = 800 μm outward (tracers move outward). The magnitude of the tracer velocities practically coincides. In the inset, we check for a possible power law behavior. The dashed line is a guide to the eye and corresponds to $|v| \propto r^{-1}$. We observe a behavior similar to that found in.[48] At small distances, data initially follow a power law with an exponent close to −1 corresponding to a radially converging or diverging flow in height restricted geometry. With increasing distances, the deviation towards lower values indicates the increasing dominance of diffusion over the directed flow.

The near quantitative agreement of the velocities points to a common driving mechanism with very similar boundary conditions. We rationalize this finding by assuming a dominant phoretic solvent flow in the regions of interest as documented by the observed power law dependence. Moreover, magnitude and sign are then controlled by the chemical potential difference corresponding to the pH change over the region of interest. For CIEX-L, this region stretches from the surface out to the far field, for AIEX-L it extends from the plateau rim to the far field, i.e. we neglect the inner region, where the height averaged pH is strongly influenced by vertical convection. Comparing with Figure 3a, one notes a pH-difference between the CIEX-L and the far field of $|\Delta pH| \approx$1.4–1.5, which agrees closely to the pH difference between the plateau and the far field for AIEX-L. Thus the magnitudes of phoretic solvent velocities coincide. However, for each case, the respective pH gradient sign determines the flow direction.

The evolution of the height averaged pH fields therefore can be qualitatively rationalized. A rigorous quantitative description could, however, not be realized within our simple analytical model. However, we saw a good agreement of the velocity curves in dependence on radius occurring for the same change in height averaged pH in Figure 3b. The velocities are determined by the corresponding drop of ground pH across the substrate. Our findings thus demonstrate that the height averaged pH is still a good qualitative approximation for the ground pH. A detailed quantitative derivation of height averaged and ground pH and the corresponding solvent velocities may be attempted in suitable finite element simulations.[26]

From centrosymmetric to complex pH fields

Modular swimmers employ CIEX. The initially centrosymmetric pH-field facilitates swimmer assembly, but becomes elliptically distorted, once the assembled swimmer starts moving. The swimmer propels at constant speed in a given direction and a stationary pH-field distortion arises. This case has already been analyzed in some detail.[9] Investigations, however, were restricted to low relative velocities by finite swimmer speed. We here address the distortion of the pH field in a homogeneous solvent flow with velocities up to v = 16 μms^{-1}. Such large solvent velocities may e.g. encountered by swimmers in the vicinity of IEX-L. Figure 4a shows a sketch of the micro-fluidic device in side view (Channel dimensions W×L×H = 10×40×2 mm^3). The inset shows a recorded pH-map of the stationary profile at v = 8 μms^{-1}. With increasing solvent velocity, the pH profiles become more elongated.

The pH profile along the solvent flow direction is shown in Figure 4b. The red line is the prediction of Eq. (S9) to (S13) calculated using input parameters determined in independently experiments (eo-pumping in quiescent solvent, PS20@CIEX45

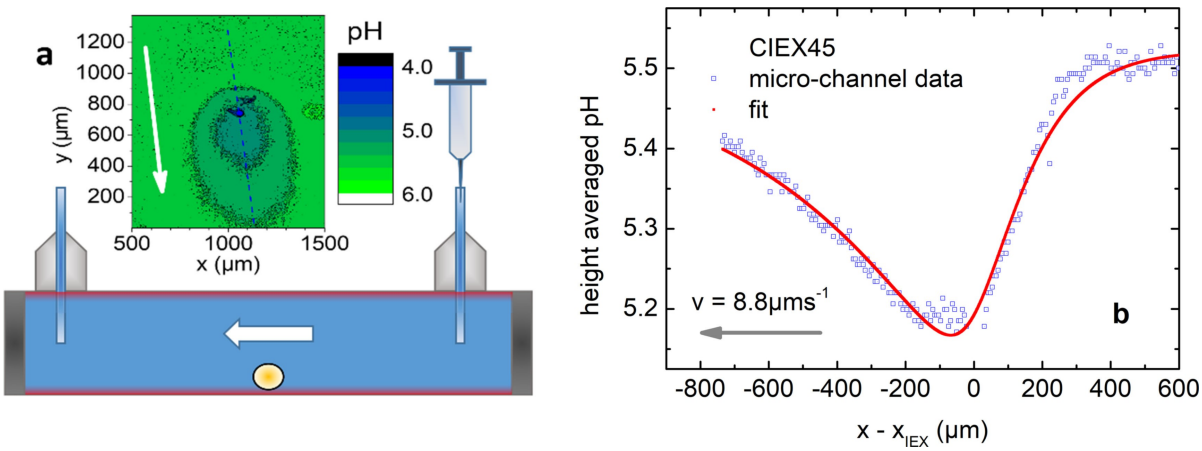

Figure 4. pH profile for IEX45 under directed flow. a) Sketch of the microfluidic channel. The inset shows the stationary pH-map recorded under flow at $v = 8.8\ \mu ms^{-1}$. The white arrow denotes the flow direction. One observes elliptically distorted iso-pH contours, with the center of the ellipses located downstream, i.e. to the back of the IEX. The dashed line denotes the location of the pH cross-section. b) pH profile taken along the dashed line in a). The solvent flow direction is indicated by the grey arrow. As compared to IEX45 at rest, the front profile is steepened, the back profile is flattened. Both parts are well described by an analytical expression.

modular swimmers) and the adjusted solvent flow velocity of $v = 8.8\ \mu ms^{-1}$. A very good description is obtained. The slight deviation in the upstream saturation region is attributed to neglect of the finite y-dimension of the channel. Equally convincing agreement was observed up to the largest investigated flow velocities of $v = 16\ \mu ms^{-1}$. This shows that for the modular swimmers the analytical description is retained even in strong homogeneous solvent flow.

Non-centrosymmetric pH landscapes can be realized by placing two or more IEX-L at different locations on the substrate. We start with a simple example. Figure 5a shows the pH map for two CIEX-L of same size placed simultaneously at a center-center distance $d = 1500\ \mu m$. The pH distribution is elongated along the center-center connection (indicated by the light blue line) with the inner region showing a saddle shape. Figure 5b displays the pH profiles taken along the center-center direction and along the perpendicular bisection. In both cases, one notes a central plateau-like, low-curvature region. This general geometry of the pH field appears to be well reproducible. It was observed in all experiments using this type of arrangement, irrespective of the CIEX-L size, their distance and the substrate type. Further, the pH fields evolved in time, but kept their symmetry. Asymmetric pH fields were observed, when the CIEX-L were placed with some time lag, or, when these were of different size. This clearly demonstrates the feasibility and facility of creating symmetric and asymmetric pH fields for swimmer steering.

An important question is, whether such a plateau arises from a linear superposition of the concentration fields applies. We addressed this point by determining the pH maps of CIEX-L pairs after a certain time of ion exchange and pH field evolution. In addition, we determined the pH map of a single CIEX-L of same size and after the same exchange time. We then calculated the concentration field for the single CIEX-L and added the same field displaced by a center-center distance d. The resulting $[H^+]$-map was re-converted to a pH map and analyzed (Figure S5b of the supplement). In this case the height averaged pH profiles both along the center-center connection and along the perpendicular bisection show a minimum. This finding is at qualitative difference to the observation made on a pair of CIEX-L. Thus no linear superposition of concentration fields applies for CIEX-L.

The pH fields around multiple sources therefore have to be determined experimentally case by case. To study the dependence of pH-field shape on CIEX-L distance we repeated the experiment for other center-center distances. With increasing distance, the central pH increases. The plateau seen in Figure 5b along the center-center connection disappears, while the profile along the perpendicular bisection flattens. We characterize this behavior by applying a linear fit to the regions lying further out on the perpendicular bisection (indicated by the dash-dotted blue lines in Figure 5b). Figure 5c shows the corresponding pH gradient dpH/dx. For too large distance we therefore approach the shape known of independent sources.

Without analytic access to the ground pH, also the solvent flow patterns have to be determined experimentally in each case. In Figure 5d, we show a map of tracer locations recorded at constant time intervals of $\Delta t = 5$ s. Small spacing between points denotes slow tracer motion. Large spacing denotes fast tracer motion. The flow field is bipolar and thus reflects the symmetry of CIEX-L placement. Most importantly, the comparison to Figure 5a shows that at any location, the tracers move perpendicular to the iso-pH contours with little angular deviations. The latter is attributed to the tracer's diffusive motion.

Tracers approaching the CIEX-L from outside the arrangement and along a direction close to that of the center-center connection behave as if approaching a single CIEX-L. They only accelerate in the converging flow field. Approaching the center-center connection along the perpendicular bisection, the tracer

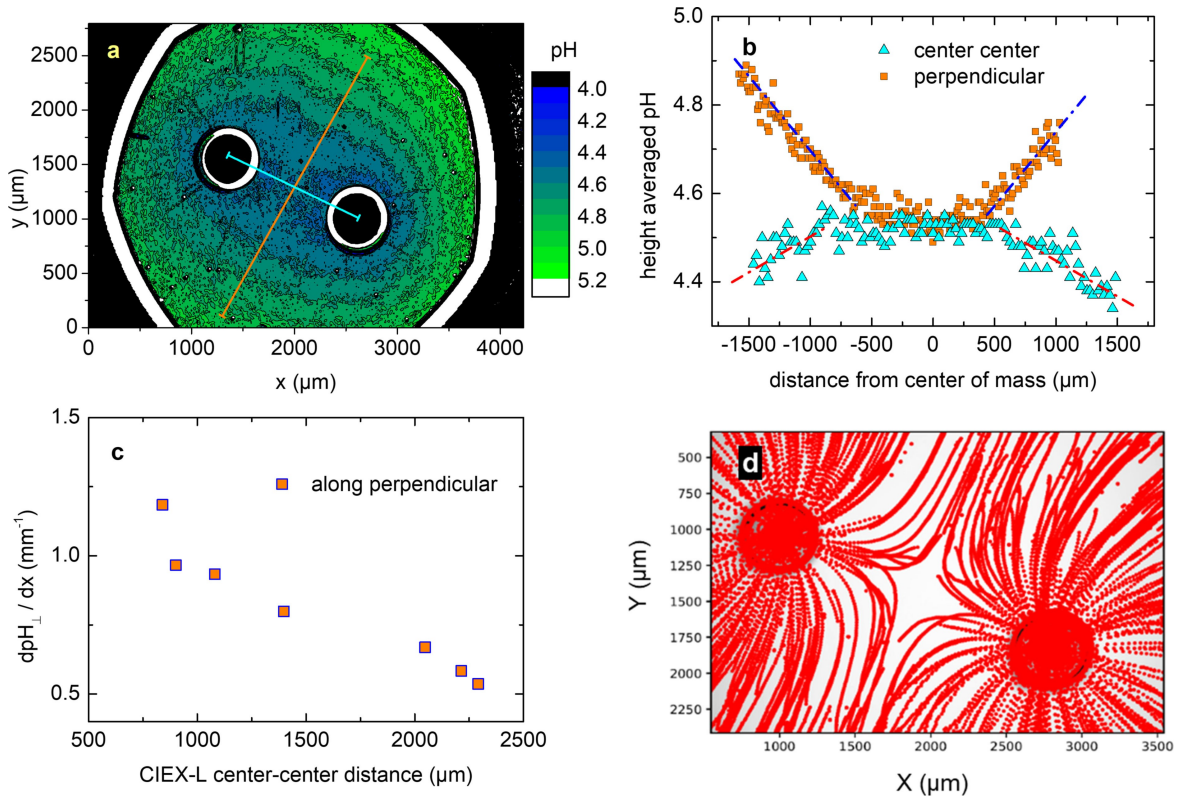

Figure 5. Results for two CIEX-L. a) Height averaged pH-map at 2560 µm center center separation as recorded at $t = 300$s. The pH-distribution takes a saddle shape. The two colored lines mark the principle directions from center to center (light blue) and perpendicular to this through the center of mass (orange). b) pH profiles along the principle directions with coloring as indicated in the key. The red (blue) dashed lines are guides to the eye to mark the regions of approximately linear pH increase and decrease along the center-center connection (perpendicular to it). c) Dependence on CIEX-L center-center distance of the pH gradient along the perpendicular direction as obtained from linear fits outside the plateau region. d) Accumulated locations of local tracer positions recorded every $\Delta t = 5$ s.

particles slow as they enter the plateau region. They then turn towards the IEX beads and accelerate again. Interestingly, we observe along this line, the tracer velocity scales linearly with the *local* pH gradient (c.f. Figure S5d in the supplement). This is somewhat unexpected, but interesting, since it would allow using the local height averaged pH gradient as proxy for the solvent flow. However, we have seen that the linear superposition of concentration fields is non-linear. Moreover, the solvent flow velocity depends on both the total drop in chemical potential from the source to the far field and the imposed flow geometry. We therefore attribute our observation to a fortuitous interplay of the named factors along this high symmetry line. In fact, when checking the relation between local pH gradient and tracer velocity no linear relation was observed at any other location. The height averaged pH thus does not generally qualify as proxy for the phoretic solvent velocity.

Adding further CIEX-L, now a large variety of pH-landscapes can be designed. A selection of representative examples and pH map videos is given in Figure S4 and Videos V1 and V2 of the electronic supplementary material. For CIEX-L arranged in polygons or circles one observes an extended pH plateau in their inside region (S4b). For CIEX-L arranged in lines the limit of a line source is approached for large CIEX-L numbers and small distances (S4c). Such line sources have also been realized from appropriately cut IEX-membranes and studied in some detail.[49] Note, however, that there different hydrodynamic boundary conditions applied, as the membranes touched both lower and upper substrates. A particular fascinating case combines a single CIEX-L with a single AIEX-L (S4d). Here, one observes a straight and narrow transition region between alkaline and acidic conditions. It shows a steep, nearly linear pH variation across the diffusively fed reaction zone, which is oriented along the perpendicular bisector to the center-center connection. Note, that in this case, the superposition of two pH fields is highly non-linear also due to the neutralization reaction (Figure S5a). This observation opens a convenient way to produce straight pH steps of arbitrary orientation at prescribed locations and may become a flexible facile alternative to pH steps formation in microfluidic like Y-junctions joining the flow of two solutions or in stop flow cells.[50]

Summarizing, our observations on multiple CIEX-L confirm the main findings of the investigation on two CIEX-L above: i) pH fields show a well-defined geometry reflecting the placement of sources. ii) This geometry is not altered in time. And iii) the solvent flow follows the direction of the height averaged pH gradient. We anticipate that this opens a facile route to

shape pH fields and solvent flow fields through appropriate choice of the geometry of the IEX placement.

Swimming in complex pH scapes

We now turn to micro-swimmers and let them propel in different pH-scapes. This section gives an overview of the large variety of trajectories realizable at different single IEX sources. We first consider Janus particles assembled at a mobile CIEX15 i.e. a low throughput pH source. In the absence of H_2O_2, the assembly behaves as a standard modular swimmer with passive cargo. The IEX-cargo distance is determined by the interplay of advective solvent flow and outward electro-phoretic motion of the cargo.[24] Its location in the back of the IEX is due to slip wind effects.[20] Thus, the fixed cargo arrangement gives the swimmer a constant propulsion speed and direction. With added H_2O_2, the behavior changes in a remarkable way. The components now form a modular swimmer with active cargo. In Figure 6a, we show a collage of images taken from video 3 in the electronic supplementary materials. The J3 cargo stays close to the mobile pump and mainly in its back with respect to the swimming direction. However, one clearly notes the vivid fluctuations in the cargo arrangement. These fluctuations are due to the J3 self-propulsion and rotational diffusivity. The cargo arrangement can also be quantitatively described in terms of effective pair potentials between IEX and cargo particles. According to the assembly model developed in,[21] cargo is trapped in a ring shaped effective pair potential well. We adapt this terminology for the present case. Slip wind effects then break the rotational symmetry of the trap and a minimum occurs to the back of the IEX.[20] Depending on its activity, J3 will explore this minimum or some larger region of the potential well by self propulsion. In Figure 6b we show the distribution of radial distances of J3 from the IEX center. The well-defined maximum demonstrates the radial J3 trapping. Despite being active, the J3 swimmers are unable to leave this "trapping region" as their velocity with regard to the IEX center is lower than that of the inward phoretic solvent flow along the substrate. While occasionally some larger excursions are seen, in general the cargo number appears to be conserved.

The Janus particles thus continuously rearrange. Hence, the phoretic slip flow at the J3 cargo surface will continuously change its direction of impact on the CIEX. This then alters the propulsion direction in a random manner. While the instantaneous velocity direction fluctuates via the cargo assembly, average propulsion direction is much more stable as the individual contributions of the J3 average out. The resulting trajectory therefore appears as a "diffusively broadened" straight trajectory or a jittered path.

Next, we consider standard modular swimmers (PS@IEX45) in the pH and flow fields of large IEX beads. In Figure 7, we show four complementary examples illustrating typical situations observed to occur quite regularly when releasing modular swimmers in the vicinity of IEX-L. These collages are taken from videos 4 to 7 of the electronic supplementary materials. In Figure 7a we show the motion of a fast swimmer (PS15@IEX45 with five first row cargo in realistic salt free suspension) near to a CIEX-L. Here, we fixed the IEXs to the top substrate, such that the flow field at the bottom plate is less pronounced in magnitude and less extended, but keeps its general shape. The fast swimmer passes with a swing. Note the slight rearrangement of cargo towards the CIEX-L. In Figure 7b, we show the motion of a similarly fast swimmer near to an AIEX-L (PS15@IEX45 with five first cargo in realistic salt free suspension, but with larger total cargo number). Again, the IEX is fixed to the top substrate. Tracer experiments in this configuration show that in addition to an overall reduced magnitude of the divergent flow field at the bottom substrate also the inner region of inward flow is missing. Despite its close encounter, the swimmer is deflected due to the outward current. Note the simultaneous outward rearrangement of the elongated cargo arrangement. In Figure 7c, we show a slow swimmer near a CIEX-L fixed to the bottom substrate (PS15@IEX45 with three first row cargo in realistic salt free suspension). Upon approaching the CIEX, the swimmer first turns toward it. As the swimmer becomes trapped, however, it obtains an outward orientation. In Figure 7d, we show a slow swimmer (PS15@IEX45 with three

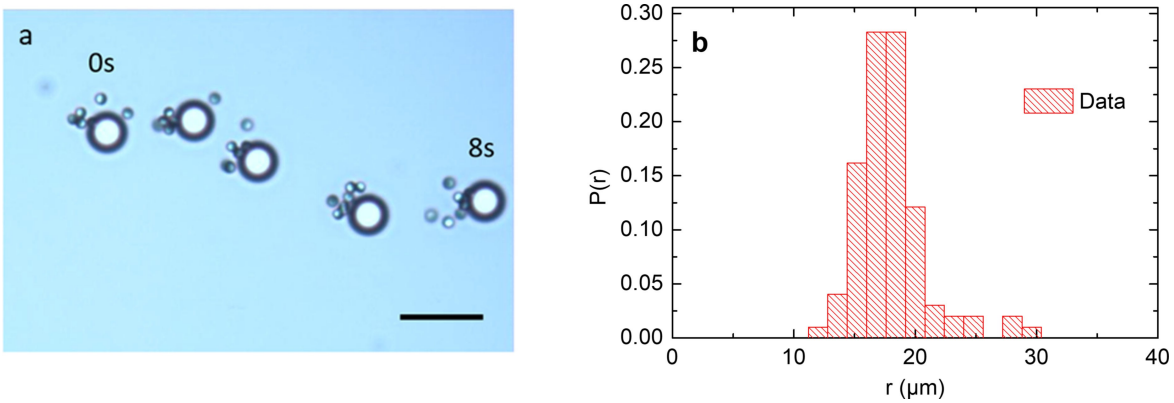

Figure 6. Tumbling drift motion of a modular micro-swimmer. a) Collage of images taken at time intervals of 2 s on J3@CIEX15 in 1% H_2O_2 solution but at otherwise realistic salt-free conditions. Scale bar: 30 μm. b) Normalized distribution of probabilities for radial distances of J3 from the IEX center as averaged over all J3 for 8 s.

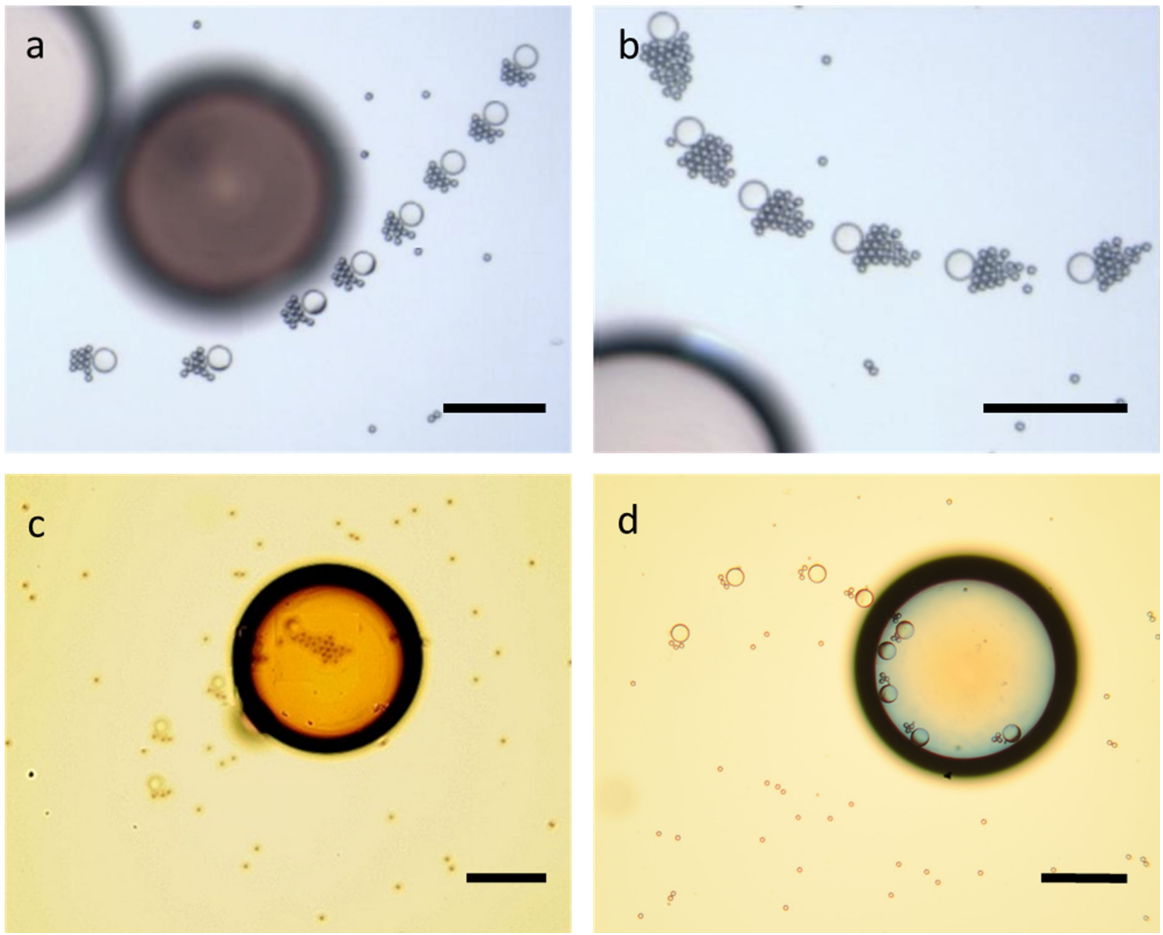

Figure 7. Examples of modular micro-swimmers propelling in pH-scapes produced by IEX-L (glass substrates, realistic deionized conditions, scale bars: 200 μm). a) PS15@CIEX45 swimming beneath a CIEX-L fixed to the upper substrate. b) PS15@CIEX45 swimming beneath an AIEX-L fixed to the upper substrate. c) PS15@CIEX45 swimming close to a CIEX-L fixed to the bottom substrate. d) PS15@CIEX45 swimming close to an AIEX-L fixed to the bottom substrate.

first row cargo in realistic salt free suspension) near an AIEX-L fixed to the bottom substrate. Here, the inner large and positive pH gradient results in a locally converging solvent flow, as expected from Figure 3b. It sweeps the swimmer towards the AIEX-L center. Once trapped, the cargo rearranges again, now more towards the center. This configuration allows for circle swimming in the effective potential well of the AIEX-L. We remark, that for AIEX-L the reaction of swimmers to the evolving pH-field is time dependent. In fact, one may observe swimmer deflection at the transition from plateau to far field pH for a short time interval after system preparation (c.f. Figure S1 and video 8 in the electronic supplementary material.

Finally, we address the case of interactions between two standard swimmers. IEX-based modular micro-swimmers carry with them a stationary and far-reaching pH field (c.f. Figure 1). As two swimmers approach each other, the pH fields will overlap, and with this also the associated phoretic flows along the substrate. This opens a fascinating toolbox to investigate swimmer encounters. Figure 8 shows two selected examples. The complete sequences can be watched in video 10 and 11 of the electronic supplementary material. In the left panels we show two PS@CIEX swimmers with initially one following suit to the other (1). After catching up (2) they temporarily form a two IEX swimmer then split to opposite directions (3) just to turn back and meet again (4). Nicely, both swimmers continuously collect fresh cargo on their way, but shed the surplus cargo in a narrow trail tracing the swimming path. In the right panel of Figure 8, we show the two PS15@CIEX45 initially approaching at an angle close to 90° with the upper one slightly lagging. As they meet, they form a single two IEX swimmer, which, however disintegrates again, and the two swimmers leave in opposing directions. The lower panel details the sequence of intermediate configurations during this encounter. pH field analysis shows that the swimmers first propel towards the lower pH regions at the other swimmer, but when reoriented after meeting and merging their pH fields, they swim towards the larger background pH.

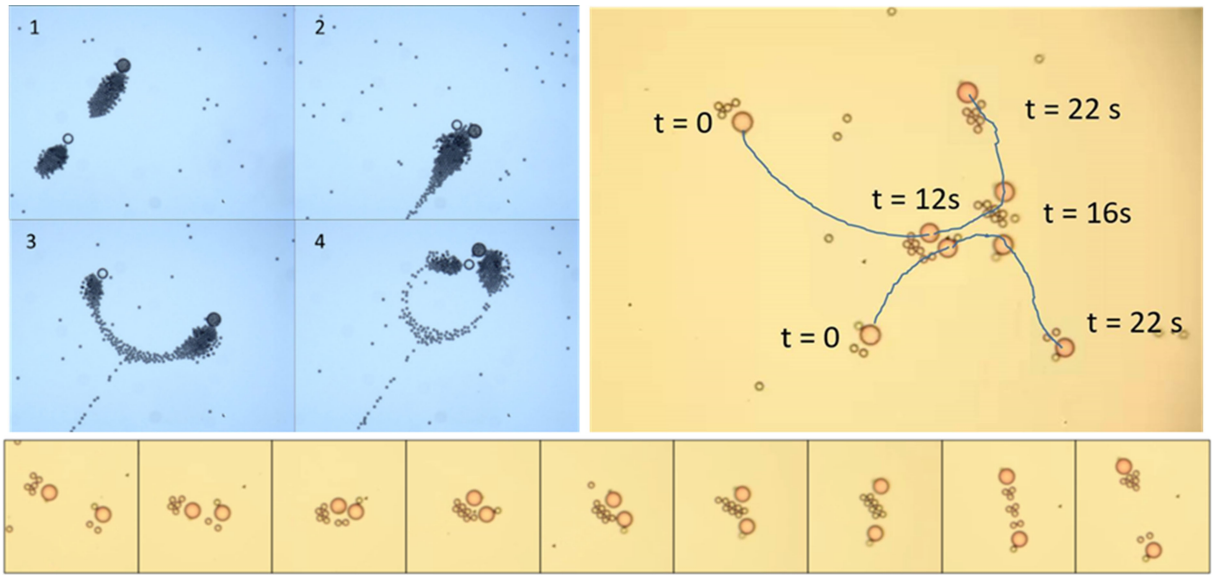

Figure 8. Swimmer-swimmer encounters. **Upper left panels**: many-cargo swimmer encounter of PS15@CIEX45 and PS15@CIEX63. Here cargo is continuously collected and shed as long lasting trail. Swimmers follow suit (1), catch up (2), divorce (3) and meet again (4). The encounter lasted for some 20s and the blue lines indicate the IEX's paths. **Right panel**: Two PS15@CIEX45 swimmers initially cross path under an approximately right angle with the lower one being slightly ahead. They merge, forming a shared cargo raft, but then divorce in opposite directions. **The bottom panel** shows further details of the configurations as they involve in time.

Discussion

To summarize, we have characterized the evolving pH fields around IEX particles in different arrangements and subjected to homogeneous solvent flow. Using tracer experiments, we investigated the corresponding global and local flow fields. The pH fields could be described by an analytical model, given advection effects stayed small and the supply of chemicals was diffusion limited. This was generally the case for small IEX particles. For larger IEX particles with high throughput of chemicals, we observed significant alterations to the pH profiles including a zone of reaction controlled pH broadening in time. There, the analytical description of profiles failed, which we attributed to the dominance of advective supply of exchangeable chemicals by localized advective currents. We succeeded, however, to characterize pH landscapes and flow fields. These mirror the symmetry of the IEX-L placement and their geometry is stable in time. The direction of the gradient of the height averaged pH provides an excellent estimate for the direction of the phoretic solvent flow. We thus demonstrated the versatility of this approach to swimmer steering by realizing several non-trivial pH landscapes and solvent flow patterns.

We then studied the motion of active and passive particles in differently shaped pH fields. Large stationary high throughput IEX-L beads create centrosymmetric pH fields similar to those previously observed for smaller, low throughput IEX, but with much stronger inward or outward flow. Standard modular swimmers move straight and carry along an elliptically distorted pH field. The same is seen for modular swimmers if the passive cargo particles are replaced with active cargo particles. Then, however, the continuous re-arrangement of the actively propelling cargo leads to jittered paths. Release of standard modular swimmers in the vicinity of IEX-L combined the effects of pH fields and solvent flows occurring on different length scales. Swimmer trajectories at single IEX-L were analyzed in some detail. Finally, we documented the chemotactic swimmer interactions due to the pH-fields produced by the swimmers themselves. Given the number of experimentally controllable boundary conditions, our survey is by no means exhaustive. In fact, many other interesting combinations remain to be realized and to be studied more systematically in future experiments. The selected observations presented are, however, ideally suited to discuss the underlying interplay of different factors governing the steering of active and passive particles in complex pH fields.

We rationalize our findings in terms of a simple heuristic model starting from the standard minimal modular swimmer model as previously proposed by Niu[23] and bearing on the description of cargo-IEX interactions in terms of effective pair potentials.[21] In Figure 9a, we draw the minimal modular swimmer of one mobile IEX assumed to be of CIEX type (yellow) and one cargo (grey) travelling straight upward (solid red arrow) across a solid substrate. Direct electrostatic interaction is neglected, though all solid surfaces are assumed to be negatively charged. The resulting Coulomb repulsion suffices to keep both cargo and IEX mobile on the like-charged substrate. It is, however, very short ranged given the elevated local salt concentration close to an IEX, and therefore it is insufficient to induce direct repulsion between IEX and cargo. The CIEX pH field is drawn as concentric blue shading, i.e. we neglect its distortion for simplicity. The solid black lines indicate two symmetric solvent streamlines as seen from the swimmer. The

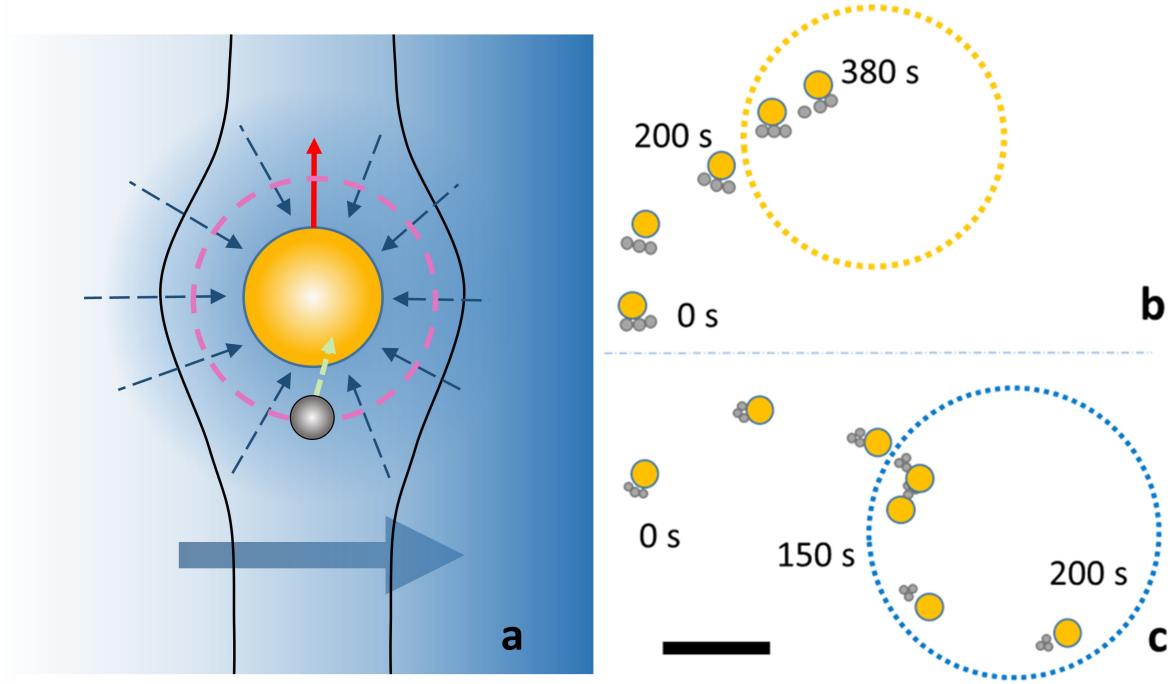

Figure 9. a) Sketch of a heuristic model to capture the observations. A swimmer propels roughly perpendicular to an imprinted global pH gradient superimposing on its own pH-field (blue background shading). The large yellow sphere denotes a mobile CIEX, the smaller grey sphere denotes the cargo in its wake. The red dashed circle indicates the location of the effective pair potential minimum. The momentary swimming direction is shown by the red solid arrow. The solid black lines denote the solvent flow line around the assembled swimmer. The other arrows denote the different types of phoretic solvent flow: pH-gradient induced global flow along the substrate (large, solid, dark blue); local flow along the substrate converging at the CIEX (dashed, dark blue); additional local solvent flow at the cargo surface (dashed, light green); The swimmer path is determined by a delicate interplay of global solvent flow, cargo position and local phoretic flow along the cargo surface. For details are described in the text. b) and c) Schematized slow swimmer locations and orientations at different elapsed times as indicated as obtained from analysis of Videos 6 and 7. b) PS15@CIEX45 in the vicinity of AIEX-L; c): PS15@CIEX45 in the vicinity of CIEX-L. Note the changing swimmer orientations.

cargo is strictly aligned in its back at the minimum of the concentric effective pair potential as induced by slip wind effects (dashed red circle).

We now superimpose a global pH field (blue shading). It may e.g. originate from some arrangement of IEX-L or a neighboring swimmer and in general may take any form. For simplicity and motivated by our profile measurements on CIEX-L, we chose it to have a constant unidirectional gradient with pH decreasing from left to right. The following solvent flows are induced, indicated by dashed arrows in Figure 9. Firstly, we have a global phoretic solvent flow with $\mathbf{v}_{ph,\ substrate}$ along the substrate to the right, i.e. closely following the pH gradient (lower dark blue arrow). Note that without anything further happening, this would not affect the swimmer orientation but simply sweep the complete assembly to the right. Second, a local solvent field around the CIEX due to its local pH field superimposing on the global one (upper dark blue arrows). Within this local inflow, the cargo is hydrodynamically trapped in the region denoted by the dashed red circle. Since the swimmer propels at constant speed, $v_{swimmer}$, the effective potential minimum along this ring is located to the back of the IEX. Consequently, the cargo is found in the back of the swimmer. However, this mirror symmetry of local inflow is additionally broken due to the non-linear, but symmetry conserving superposition of the global flow. Correspondingly, the minimum of the potential well shifts counter-clockwise. A third effect is more subtle. The resulting local pH gradient now is at a different angle to the propulsion direction. Thus, also the local phoretic slip at the cargo surface, $\mathbf{v}_{ph,\ particle}$, (bright green arrow) changes orientation and to a lesser degree also magnitude. With the cargo trapped to the potential well, this induces a clockwise drag of the cargo along the well.

Thus, dominant global solvent flow can induce a left turn in Figure 9, while a dominant altered local pH gradient can induce a right turn. However, at the same time, the slip wind effect still works towards keeping the cargo in place and stabilize the momentary swimming direction. In most experiments wind slip dominated. Nevertheless, cargo rearrangement under the influence of the broken mirror symmetry of phoretic solvent flow was frequently seen to interfere. In Figure 7a, the cargo is displaced by the global inflow towards the CIEX-L, which assists the successful swing by maneuver. In Figure 7b it is displaced away from the AIEX-L by the global outflow. This was insufficient to trigger a catch, but presumably stretched the deflection process.

In Figure 7c and d we show swimmers of lower cargo number. For clarity, we have redrawn their positions and orientations in Figure 9b and c. Their speeds are lower. Hence, wind slip effects are diminished and the cargo can be rearranged more easily. In both experiments, the global

phoretic solvent flow is directed towards the respective IEX-L. However, the cargo is displaced away from the IEX-L during the (initial) approach. Here, the change of the local phoretic slip direction at the cargo surface in the strong imprinted pH gradient dominates the effect of asymmetric local flow fields. In the final phases of the catch, however, the situation changes. Both swimmers enter the effective swimmer – IEX-L pair potential well. While radial swimmer motion ceases, the global solvent inflow does not. For the swimmer at the CIEX-L it dominates and sweeps the cargo even further towards the CIEX-center. There, the CIEX-L pH gradient is too weak to counteract (c.f. Figure 3a). The swimmer orientation is dictated by the hydrodynamics in the geometric confinement between substrate and CIEX-L sphere. The smaller cargo is swept closer to the CIEX-L center than the larger CIEX45 (c.f. Figure S5a). In principle, such an orientation is ideally suited for an escape attempt. Due to the weak pH gradient, however, the propulsion velocity is much smaller than the inflow velocity. The swimmer stays stuck with its back towards the IEX center. At slower inflows, sufficient propulsion speed and suitable orientation, we occasionally witnessed a successful escape from the trap at the IEX. An example is shown in video 11 of the electronic supplementary material. Escape, however, is frequent after encounter and merging of individual swimmers (Figure 7). Also there it involves initial attraction and rearrangement of cargo in the incoming global flow now shared between two CIEX. The corresponding pH- and flow field should be similar to that shown in Figure 5a and 5d, respectively. The cargo settles in between. Then, it is the cargo closest to each CIEX propelling the newly forming swimmers in opposite directions.

A particularly interesting behavior was observed in the experiment of Figure 7d for the CIEX swimmer trapped under an AIEX-L (redrawn in Figure 9c). Upon arrival, the CIEX was swept a fair way underneath the AIEX-L, but then returned to a position closer to the AIEX rim. This was assisted by the concurring cargo motion. The cargo first was swept inward even further than the IEX. This is similar to the case observed in 7c. In its new position, the pH local gradient is tilted away from the radial coordinate towards the CIEX. Therefore, the phoretic slip along the cargo surface has a finite component, oriented in CIEX direction. This drives the swimmer back again in the outward direction until the arrangement stabilizes. There, the global pH gradient is steep. The inflow induced inward reorientation of cargo is now balanced by the gradient induced outward reorientation. This yields a slight inward displacement of cargo. The swimmer is thus trapped in the concentric swimmer-AIEX pair interaction well with the cargo location stabilized in the competition of all three flow effects. This, however, is a suitable orientation for propulsion along the well.

We emphasize that this situation of circle swimming was reached by self organization and balance of competing global and local flows and the resulting circular swimmer motion is not a direct result of mechanical confinement. It is conceivable that given the right combination of swimmer speed, global solvent inflow and distance dependent radial pH gradient circular orbits can be achieved also further out.

Finally, we consider the case of swimmer-swimmer interactions. Here the details, in particular of divorce, are fairly complicated and need further systematic study. Already now, however, our observation also has an important message concerning the guidance of modular micro-swimmers: In the experiment of Figure 8 no strong advection is present. This, therefore, is no necessary condition for swimmer steering. In fact, re-orientation of the slip velocity direction at the cargo surface depends on the local ∇pH, being a superposition of the global pH field with that of the swimmer IEX. It thus is an example of logarithmic sensing,[51] which is prominent and important in many biological swimmer systems.[52] Thus, the sculpturing of complex pH landscapes does not necessarily involve the use of IEX-L. Use of smaller IEX should suffice to guide modular swimmers and at the same time keep the effort for system characterization low. Nevertheless, one might for practical reasons (exchange capacity, steeper gradients, height dependent flow pattern etc.) still prefer working with IEX-L. In any case, we believe that our study comprising measurements and observations on different IEX types, sizes and locations will aid the development of further qualitative and quantitative modelling. However, theoretical attempts along this line as well as simulations will also need further experimental input.

Conclusion

We constructed pH fields of non-trivial geometry from combinations of cationic and anionic ion exchange beads. These were characterized in detail using two-channel photometry. We then studied the motion of passive tracers and of phoretic swimmers in such pH-fields. For swimmers, we reported swimmer trapping and escape, trajectory deflection as well as swing-by maneuvers, and – most intriguingly – also stable, self-organized, circular orbits. To rationalize our observations, we extended Niu's propulsion model developed for a single passive cargo in the wake of a single CIEX by combining it with a constant unidirectional pH-gradient.[25] We argued that swimmer trajectories were determined by different factors. The first is the complex shapes of the pH fields. These arise from the competition between diffusive and advective transport of chemicals over different length scales and their accumulation or consumption in follow-up reactions. They strongly depend on the rate of ion exchange. The second is the resulting non-trivial 3D flow pattern. It arises from the competing global and local phoretic solvent flows as triggered by the local and global pH-gradients. Our improved heuristic model allowed rationalizing some of our key observations concerning swimmer trajectories. A deeper investigation of swimmer-IEX-L interactions and the chemo-taxis like effects seen in swimmer-swimmer encounters was beyond the scope of the present investigation and is left for a forthcoming study.

Further extension and application appears to be straightforward for both our approach and our model. One may address active cargo or cargo of mixed sizes as well as combinations involving multiple CIEX, anisometric CIEX splinters or combinations involving AIEX and CIEX. In their pH fields of even more

complex geometry the stabilization of other types of trajectories can be envisioned. For example a sinusoidal swimmer motion in the center of two complementary rows of alternating AIEX-L and CIEX-L. Another important point not yet addressed is random rearrangement of cargo as e.g., seen for the J3 in Figure 6. While we expect it to destabilize circular orbits, it surely will help escaping local traps. With improved spatial and temporal resolution of the employed optical techniques (and possibly the inclusion of 3D flow and pH mapping) our approach may in future address also single component phoretic swimmers, e.g. Janus swimmers. Also there, we expect the same interplay of local and global solvent flows, but with faster reactions, steeper gradients and on smaller scales.

The highly desired step from qualitative to quantitative modelling appears to be more demanding. Our study was performed on model systems, which allowed for detailed characterization of all components and experimental boundary conditions. However, comprehensive systematic experiments are still needed to provide a reliable database for future quantitative modelling. Moreover, the development of suitable analytical descriptions as well as of simulation algorithms remains a formidable challenge.

Our study clearly demonstrates the feasibility and the potential of swimmer steering by externally imposed chemical structuring. This appears particularly interesting in view of biological environments. There, charged surfaces and chemically reactive sites lead to an abundancy of complex chemical fields with spatially and temporarily varying gradients. We anticipate that our study may contribute to a better qualitative understanding of the phoretic contribution to solvent motion, setting the boundary conditions for advective and diffusive and phoretic molecular and colloidal transport also in biological systems.

Acknowledgements

We thank Denis Botin for contributing to particle and surface characterizations. We thank Larysa Barbaran for the kind gift of well characterized Janus particles. Numerous fruitful discussions on experimental issues and gradient modelling with Stanislav Khodorov, Frank Siebers, Julian Weber, Andreas Fischer, Thomas Speck, Hartmut Löwen, Christian Holm and Joost de Graaf greatly advanced the present work. This work was financially supported by the Max Planck Graduate Center with the Johannes Gutenberg-Universität Mainz (MPGC). N.M is fellow of the MPGC. Financial Support of the DFG in the priority program SPP 1726 (Grant Nos. Pa 459/18-1,2) is gratefully acknowledged. Open Access funding enabled and organized by Projekt DEAL.

Conflict of Interest

The authors declare that they have no conflict of interest.

Data Availability Statement

Original data are available from the corresponding author upon reasonable request.

Keywords: Microswimming · Diffusio-phoresis · pH Microphotography · Microfluidics · Ion-Exchange

[1] J. L. Anderson, D. C. Prieve, *Sep. Purif. Rev.* **1984**, *13*, 67–103.
[2] J. L. Anderson, *Ann. Rev. Fluid Mech.* **1989**, *21*, 61–99.
[3] Á. V. Delgado, F. Carrique, R. Roa, E. Ruiz-Reina, *Curr. Op. Coll. Interf. Sci.* **2016**, *24*, 32–43.
[4] D. Botin, F. Carrique, E. Ruiz-Reina, T. Palberg, *J. Chem. Phys.* **2020**, *152*, 244902. https://doi.org/10.1063/5.0010692.
[5] A. Würger, *Rep. Prog. Phys.* **2010**, *73*, 126601.
[6] F. M. Weinert, C. B. Mast, D. Braun, *Phys. Chem. Chem. Phys.* **2011**, *13*, 9918–9928.
[7] H. Jiang, N. Yoshinaga, M. Sano, *Phys. Rev. Lett.* **2010**, *105*, 268302.
[8] D. Velegol, A. Garg, R. Guha, A. Kar, M. Kumar, *Soft Matter* **2016**, *12*, 4686–4703.
[9] N. Möller, B. Liebchen, T. Palberg, *Eur. Phys. J. E* **2021**, *44(3)*, 1–17.
[10] J. L. Moran, P. M. Wheat, J. D. Posner, *Phys. Rev. E* **2010**, *81*, 065302(R).
[11] W. Duan, W. Wang, S. Das, V. Yadav, T. E. Mallouk, A. Sen, *Annu. Rev. Anal. Chem.* **2015**, *8*, 311–333.
[12] J. L. Moran, J. D. Posner, *Annu. Rev. Fluid Mech.* **2017**, *49*, 511–540.
[13] C. Kurzthaler, C. Devailly, J. Arlt, T. Franosch, W. C. K. Poon, V. A. Martinez, A. T. Brown, *Phys. Rev. Lett.* **2018**, *121*, 078001.
[14] C. Zhou, H. P. Zhang, J. Tang, W. Wang, *Langmuir* **2018**, *34*, 3289–3295.
[15] X. Chen, C. Zhou, W. Wang, *Chem. Asian J.* **2019**, *14*, 2388–2405.
[16] T. Speck, *Phys. Rev. E* **2019**, *99*, 060602(R).
[17] J. Sachs, S. N. Kottapalli, P. Fischer, D. Botin, T. Palberg, *Colloid Polym. Sci.* **2021**, *299*, 269–280.
[18] R. Niu, T. Palberg, *Soft Matter* **2018**, *14*, 7554–7568.
[19] R. Niu, S. Khodorov, J. Weber, A. Reinmüller, T. Palberg, *NJP* **2017**, *19*, 115014.
[20] R. Niu, D. Botin, A. Reinmüller, T. Palberg, *Langmuir* **2017**, *33*, 3450–3457.
[21] R. Niu, T. Palberg, T. Speck, *Phys. Rev. Lett.* **2017**, *119*, 028001.
[22] A. Reinmüller, H. J. Schöpe, T. Palberg, *Langmuir* **2013**, *29*, 1738–1742.
[23] R. Niu, A. Fischer, T. Palberg, T. Speck, *ACS Nano* **2018**, *12*, 10932–10938.
[24] B. Liebchen, R. Niu, T. Palberg, H. Löwen, *Phys. Rev. E* **2018**, *98*, 052610.
[25] A. A. Farniya, M. J. Esplandiu, D. Reguera, A. Bachtold, *Phys. Rev. Lett.* **2013**, *111*, 168301.
[26] R. Niu, P. Kreissl, A. T. Brown, G. Rempfer, D. Botin, C. Holm, T. Palberg, J. de Graaf, *Soft Matter* **2017**, *13*, 1505–1518.
[27] M. Ibele, T. E. Mallouk, A. Sen, *Angew. Chem. Int. Ed.* **2009**, *48*, 3308.
[28] W. Duan, M. Ibele, R. Liu, A. Sen, *Eur. Phys. J. E* **2021**, *35*, 77.
[29] M. E. Ibele, P. E. Lammert, V. H. Crespi, A. Sen, *ACS Nano* **2010**, *4*, 4845–485.
[30] A. Aubret, M. Youssef, S. Sacanna, J. Palacci, *Nature Phys. Sci.* **2018**, *14*, 1114–1118.
[31] C. Zhou, X. Chen, Z. Han, W. Wang, *ACS Nano* **2019**, *13*, 4064–4072.
[32] C. Lozano, B. ten Hagen, H. Löwen, C. Bechinger, *Nat. Commun.* **2016**, *7*, 12828.
[33] J. Simmchen, J. Katuri, W. Uspal, M. N. Popescu, M. Tasinkevych, S. Sánchez, *Nat. Commun.* **2016**, *7*, 10598.
[34] A. F. Demirörs, M. T. Akan, E. Poloni, A. R. Studart, *Soft Matter* **2018**, *14*, 4741–4749.
[35] L. Niese, L. Wang, S. Das, J. Simmchen, *Soft Matter* **2020**, *16*, 10585–10590.
[36] B. Liebchen, H. Löwen, in *Chemical Kinetics Beyond the Textbook*, K. Lindenberg, R. Metzler, G. Oshanin (Eds.) World Scientific, **2019** pp. 493–516.
[37] J. X. Chen, Y. G. Chen, Y. Q. Ma, *Soft Matter* **2016**, *12*, 1876–1883.
[38] J. X. Chen, Y. G. Chen, R. Kapral, *Adv. Sci.* **2018**, *5*, 1800028.
[39] R. Cui, Q. H. Chen, J. X. Chen, *Nanoscale* **2020**, *12*, 12275–12280.
[40] A. T. Brown, W. C. K. Poon, C. Holm, J. de Graaf, *Soft Matter* **2017**, *13*, 1200–1222.
[41] M. N. Popescu, W. E. Uspal, A. Dominguez, S. Dietrich, *Acc. Chem. Res.* **2018**, *51*, 2991–2997.

[42] M. J. Esplandiu, K. Zhang, J. Fraxedas, B. Sepulveda, D. Reguera, *Acc. Chem. Res.* **2018**, *51*, 1921–1930.
[43] Z. Y. Xiao, M. Wei, W. Wang, *ACS Appl. Mater. Interfaces* **2019**, *11*, 6667–6684.
[44] F. J. Millero, *Geochim. Cosmochim. Acta.* **1995**, *59*, 661–677.
[45] F. J. Millero, R. Feistel, D. G. Wright, T. J. McDougall, *Deep-Sea Res. Part I* **2008**, *55*, 50–72.
[46] L. Baraban, M. Tasinkevych, M. N. Popescu, S. Sanchez, S. Dietrich, O. G. Schmidt, *Soft Matter* **2012**, *8(1)*, 48–52.
[47] D. Botin, J. Wenzl, R. Niu, T. Palberg, *Soft Matter* **2018**, *14(40)*, 8191–8204.
[48] R. Niu, T. Palberg, *Soft Matter* **2018**, *14.18*, 3435–3442.
[49] M. J. Esplandiu, D. Reguera, J. Fraxeidas, *Soft Matter* **2020**, *16*, 3717–3726.
[50] K. Shinohara, Y. Sugii, A. Hibara, M. Tokeshi, T. Kitamori, K. Okamoto, *Exp. Fluids* **2004**, *38*, 117–122.
[51] J. Palacci, B. Abécassis, C. Cottin-Bizonne, C. Ybert, L. Bocquet, *Soft Matter* **2010**, *8*, 980–994.
[52] U. B. Kaupp, L. Alvarez, *Eur. Phys. J. Special Topics* **2016**, *225*, 2119–2139.

Manuscript received: May 10, 2021
Revised manuscript received: June 18, 2021
Accepted manuscript online: July 15, 2021
Version of record online: August 4, 2021